Photoactive Metal Carbonyl Complexes Bearing N-Heterocyclic Carbene Ligands: Synthesis, Characterization and Viability as Photoredox Catalysts

Meiqiong Tang,[a] Lee Cameron,[b] Eve M. Poland,[a] Li-Juan Yu,[c] Stephen A. Moggach,[d] Rebecca O. Fuller,[a] Hai Huang,[e] Jianwei Sun,[e,f] Stuart C. Thickett,[a] Massimiliano Massi,[b] Michelle L. Coote,[c]* Curtis C. Ho,[a]* and Alex C. Bissember[a]*

[a] School of Natural Sciences – Chemistry, University of Tasmania, Hobart, Tasmania 7001, Australia

[b] School of Molecular and Life Sciences, Curtin University, Perth, Western Australia 6102, Australia

[c] Research School of Chemistry, Australian National University, Canberra, Australian Capital Territory 2601, Australia

[d] School of Molecular Sciences, University of Western Australia, Perth, Western Australia 6009, Australia

[e] Jiangsu Key Laboratory of Advanced Catalytic Materials & Technology, School of Petrochemical Engineering, Changzhou University, Changzhou, China

[f] Department of Chemistry, The Hong Kong University of Science and Technology, Clear Water Bay, Kowloon, Hong Kong SAR, China

ABSTRACT: This report details the synthesis and characterization of a small family of previously unreported, structurally-related chromium, molybdenum, tungsten, manganese, and iron complexes bearing N-heterocyclic carbene and carbonyl supporting ligands. These complexes have the general form $[ML(CO)_3X]$ or $[ML(CO)_3]$, where X = CO or Br and L = 1-phenyl-3-(2-pyridyl)imidazolium. Where possible, the solid state, spectroscopic, electrochemical, and photophysical properties of these molecules were studied using a combination of experiment and theory. Photophysical studies reveal that decarbonylation occurs when these complexes are exposed to ultraviolet light, with the CO ligand being replaced with a labile CH_3CN solvent molecule. To obtain insights into the potential utility, scope, and applications of these complexes in visible-light-mediated photoredox catalysis, their capacity to facilitate a range of photoinduced reactions via the reductive or oxidative functionalization of organic molecules was investigated. These chromium, molybdenum, and manganese catalysts efficiently facilitated atom-transfer radical addition processes. In light of their photolability, these types of catalysts may potentially allow for the development of photoinduced reactions involving less conventional inner-sphere electron transfer pathways.

INTRODUCTION

Since 2008, visible-light-mediated photoredox catalysis has enjoyed a renaissance that has extended the applications of radical chemistry in organic synthesis and increased the capacity to functionalize molecules under mild conditions.[1] Despite these advances, the overwhelming majority of transformations employing transition-metal-based photoredox catalysts continue to rely on the reactivity provided by precious ruthenium and iridium systems rather than exploiting cheaper and earth abundant metals.[2] Consequently, the development of alternative photoredox catalysts that comprise first row or less conventional transition metals are required and remain of both fundamental and more applied interest. A selection of known chromium, molybdenum, tungsten, manganese, and iron-based photoredox catalysts are provided in Figure 1a.[3–7]

Various photoactive tricarbonyl rhenium(I) N-heterocyclic carbene (NHC) complexes have been reported (Figure 1b).[8] For example, we recently identified the viability of rhenium(I) tricarbonyl complexes, including those bearing NHC ligands, as versatile photoredox catalysts.[9] While rhenium is a rare metal, we thought that the structural motif featured in complex **F** could be employed to prepare analogous photoactive complexes using other metals. Specifically, we anticipated that this approach might allow us to broaden the scope of earth abundant and/ or less established transition metal systems in photoredox catalysis. To this end, we prepared a small family of chromium, molybdenum, tungsten, manganese, and iron complexes **1**–**5** (Figure 1c) that are structurally related to rhenium(I) NHC analogue **F**.[10] We studied their respective structures in the solid state, investigated their photophysical and electrochemical properties, and comprehensively evaluated their capacity to serve as photoredox catalysts across a wide range of representative transformations. The findings of this research are presented and discussed herein.

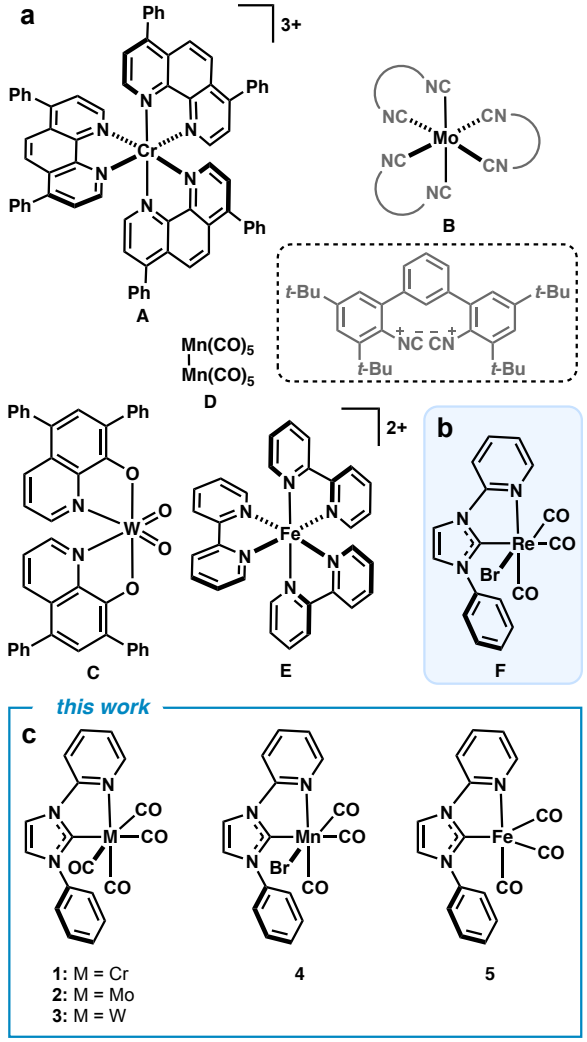

Figure 1. (**a**) Representative examples of reported chromium-, molybdenum-, tungsten-, manganese-, and iron-based photoredox catalysts **A**–**E**. (**b**) Reported rhenium(I) photoredox catalyst **F**. (**c**) Original complexes **1**–**5** prepared in this study.

EXPERIMENTAL SECTION

General Information. NMR spectroscopic experiments were performed on a Bruker Avance III NMR spectrometer operating at 300 MHz (^{1}H) and 75 MHz (^{13}C), Bruker Avance III NMR spectrometer operating at 400 MHz (^{1}H) and 100 MHz (^{13}C) or on a Bruker Avance III NMR spectrometer operating at 600 MHz (^{1}H) and 150 MHz (^{13}C). The deuterated solvents used were $CDCl_3$, CD_3CN, and DMSO-d_6. Chemical shifts were recorded in ppm. Spectra were calibrated by assignment of the residual solvent peak to δ_H 7.26 and δ_C 77.16 for $CDCl_3$, δ_H 1.94 and δ_C 1.32 for CD_3CN, and δ_H 2.50 and δ_C 39.52 for DMSO-d_6. Coupling constants (J) were recorded in Hz. Infrared spectroscopy was performed on a Shimadzu FTIR 8400s spectrometer, with samples analyzed as CH_2Cl_2 or MeCN solutions in NaCl cells. Elemental analyses were conducted using a Thermo Finnigan EA 1112 Series Flash Elemental Analyzer. Photoredox catalysis experiments were performed in a custom blue LED (λ_{max} = 467 nm) photoreactor (blue LED strips were purchased from aliexpress.com),[11] or using a 15-W white LED lamp (lamp diameter: 120 mm; 450–460 nm), or a 15-W blue LED lamp (lamp diameter: 120 mm; 460–480 nm) with fan cooling. In each experiment, reaction vessels were placed within 3–4 cm from the light source; light filters were not used. All irradiation vessels were composed of borosilicate glass.

TLC was performed using Merck silica gel 60-F_{254} plates. Developed TLC plates were visualized by UV absorbance (254 nm) or through application of heat to a plate stained with cerium molybdate {$Ce(NH_4)_2(NO_3)_6$, $(NH_4)_6Mo_7O_{24}{\cdot}4H_2O$, H_2SO_4, H_2O}. Flash column chromatography was performed with flash grade silica gel (60 μm) and the indicated eluent in accordance with standard techniques.[12] THF, MeOH, Et_2O, $CHCl_3$, CH_2Cl_2, PhMe, DMF, and CH_3CN were de-aerated via a nitrogen sparge then dried using an Innovative Technology solvent purification system. Unless otherwise specified all reagents employed in these studies were used as received from Sigma-Aldrich, AK Scientific, Combi-Blocks, and Oakwood. Previously reported 1-phenyl-3-(2-pyridyl)imidazolium bromide was prepared according to a literature procedure.[8b] Et_3N was dried over KOH and distilled prior to use.

General Procedure A: Synthesis of Complexes 1–4. In an oven-dried Schlenk flask, 1-phenyl-3-(2-pyridyl)imidazolium bromide (300 mg, 0.99 mmol) and metal carbonyl (1 equiv, 0.99 mmol) was dried under vacuum and backfilled with argon. PhMe (8 mL) was added followed by Et_3N (5 equiv, 0.7 mL, 5.00 mmol) and the mixture was heated at reflux. After 72 h, the mixture was cooled to room temperature, and then H_2O (15 mL) and hexanes (15 mL) were added. The solids were collected via vacuum filtration, washed with hexanes, dissolved in CH_2Cl_2 then passed through a Celite® and acidic alumina plug. The filtrate was collected and concentrated under reduced pressure to leave a brightly colored powder. Crystals suitable for a single crystal X-ray diffraction were grown after slow evaporation from CH_3CN.

*Synthesis of complex **1***. Reaction using [$Cr(CO)_6$] and following General Procedure A. Previously unreported complex **1** was obtained as a light-orange solid (119 mg, 31% yield). Mp: 204 °C dec. ^{1}H NMR (600 MHz, DMSO-d_6) δ 8.81 (d, J = 5.4 Hz, 1H), 8.70 (d, J = 1.9 Hz, 1H), 8.13–8.12 (m, 2H), 7.90 (d, J = 1.9 Hz, 1H), 7.63–7.59 (m, 4H), 7.53 (t, J = 7.0 Hz, 1H) 7.36 (q, J = 5.2 Hz, 1H) ppm. ^{13}C{^{1}H} NMR (150 MHz, DMSO-d_6) δ 228.9, 228.5, 217.5, 209.7, 153.4, 152.9, 140.5, 140.4, 129.9, 129.3, 127.0, 126.6, 122.6, 118.1, 112.5 ppm. IR (CH_2Cl_2) 2003 (CO), 1892 (CO), 1836 (CO) cm^{-1}. Anal. Calcd for $C_{18}H_{11}CrN_3O_4$: C, 56.11; H, 2.88; N, 10.91. Found: C, 56.29; H, 2.65; N, 11.06.

*Synthesis of complex **2***. Reaction using [$Mo(CO)_6$] and following General Procedure A. Previously unreported complex **2** was obtained as a bright-yellow solid (313 mg, 73% yield). Mp: 161 °C dec. ^{1}H NMR (600 MHz, DMSO-d_6) δ 8.77 (d, J = 5.2 Hz, 1H), 8.67 (s, 1H), 8.27-8.18 (m, 2H), 7.98 (s, 1H), 7.68 (d, J = 7.9, 2H), 7.52 (t, J = 7.7 Hz, 2H), 7.52 (t, J = 7.3 Hz, 1H), 7.43 (t, J = 5.9 Hz, 1H) ppm. ^{13}C{^{1}H} NMR (150 MHz, DMSO-d_6) δ 223.1, 221.1, 207.5, 201.7, 153.1, 152.6, 141.0, 140.4, 129.8, 129.0, 125.8, 123.1, 122.7, 118.9, 113.4 ppm. IR (CH_2Cl_2) 2010 (CO), 1900 (CO), 1838 (CO) cm^{-1}. Anal. Calcd for $C_{18}H_{11}MoN_3O_4$: C, 50.36; H, 2.58; N, 9.79. Found: C, 50.18; H, 2.40; N, 9.95.

*Synthesis of complex **3***. Reaction using [$W(CO)_6$] and following General Procedure A. Previously unreported complex **3** was obtained as a bright-orange solid (205 mg, 40% yield). Mp: 165 °C dec. ^{1}H NMR (600 MHz, DMSO-d_6) δ 8.92 (d, J = 4.9 Hz, 1H), 8.70 (s, 1H), 8.30–8.24 (m, 2H), 7.98 (s, 1H), 7.67 (d, J = 7.5 Hz, 2H), 7.61 (t, J = 7.4 Hz, 2H), 7.54 (t, J = 7.2 Hz, 1H), 7.43 (t, J = 6.1 Hz, 1H) ppm. ^{13}C{^{1}H} NMR (150 MHz,

DMSO-d_6) δ 215.9, 214.0, 202.0, 190.2, 153.5, 153.4, 141.1, 140.2, 129.8, 129.0, 126.1, 125.9, 123.6, 118.9, 113.5 ppm. IR (CH_2Cl_2) 2004 (CO), 1889 (CO), 1836 (CO) cm^{-1}. Anal. Calcd for $C_{18}H_{11}N_3O_4W$: C, 41.81; H, 2.14; N, 8.12. Found: C, 41.86; H, 2.09; N, 8.27.

Synthesis of complex ***4***. Reaction using [$MnBr(CO)_5$] and following General Procedure A. Previously unreported complex **4** was obtained as a dark-yellow solid (176 mg, 40% yield). Mp: 178 ˚C dec. ^{1}H NMR (600 MHz, DMSO-d_6) δ 8.94 (d, J = 5.4 Hz, 1H), 8.69 (s, 1H), 8.25 (s, 2H), 7.99 (s, 1H), 7.72–7.71 (m, 2H), 7.65 (t, J = 7.4 Hz, 2H), 7.61–7.59, (m, 1H), 7.52 (q, J = 5.3 Hz, 1H) ppm. ^{13}C{^{1}H} NMR (150 MHz, DMSO-d_6) δ 222.7, 221.4, 217.4, 202.7, 153.4, 153.2, 152.5, 141.2, 139.4, 129.6, 126.7, 126.6, 123.1, 117.7, 112.5 ppm. IR (CH_2Cl_2) 2023 (CO), 1940 (CO), 1911 (CO) cm^{-1}. Anal. Calcd for $C_{17}H_{11}BrMnN_3O_3$: C, 46.39; H, 2.52; N, 9.55. Found: C, 46.69; H, 2.51; N, 9.71.

Synthesis of complex ***5***. In an oven-dried Schlenk flask, 1-phenyl-3-(2-pyridyl)imidazolium bromide (300 mg, 0.99 mmol) and [$Fe(CO)_5$] (194 mg, 1 equiv, 0.99 mmol) were dried under vacuum and backfilled with argon. PhMe (8 mL) was added followed by Et_3N (5 equiv, 0.7 mL, 5.0 mmol) and the mixture heated at reflux. After 72 h, the mixture was cooled to room temperature and the resulting solids collected via cannula filtration. The solids were dried in vacuo and stored in a Schlenk flask under an argon atmosphere. Previously unreported complex **5** was obtained as a dark-purple powder (50 mg, 13% yield). Crystals suitable for a single crystal X-ray diffraction study were grown after slow evaporation from PhMe. NMR spectroscopic analysis could not be performed due to the paramagnetic nature of complex **5**. IR (CH_2Cl_2 solution) 1980 (CO), 1902 (CO), 1887 (CO) cm^{-1}. Anal. Calcd for $C_{17}H_{11}FeN_3O_3{\cdot}H_2O$: C, 53.85; H, 3.46; N, 11.08. Found: C, 54.16; H, 3.19; N, 11.54.

General Procedure B: Reaction Shown in Table 4. In a nitrogen-filled glovebox (in the dark), 4-methoxystyrene (**7**) {13.8 µL, 100 µmol; 4-methoxystyrene (neat) was passed through a silica gel plug prior to use}, *N*-chloro-*N*-methyl-*p*-toluenesulfonamide (33 mg, 150 µmol), and the photocatalyst (1.0 µmol; 2 mL of a 0.5 mM solution in DCE) were successively added to a 4-mL glass vial containing a stir bar. This vial was then capped and placed in the blue LED photoreactor and magnetically stirred. The vial was irradiated while maintained at 25 °C. After 24 h, the vial was removed from the photoreactor, the reaction mixture was filtered through a silica plug, and the organic solvent was concentrated under reduced pressure. Yields were determined by ^{1}H NMR spectroscopy using an internal standard (CH_2Br_2).

General Procedure C: Reaction Shown in Scheme 2a. In air (in the dark), (*E*)-3-(2-isocyanophenyl)acrylonitrile (**9**) (10 mg; 65 µmol), phenylglyoxylic acid (15 mg; 100 µmol), K_2HPO_4 (18 mg, 100 µmol), photocatalyst (1.0 µmol), and DMF (500 µL) were successively added to a 4-mL glass vial containing a stir bar. This vial was then capped and placed in the blue LED photoreactor and magnetically stirred. The vial was irradiated while maintained at 25 °C. After 24 h, the reaction mixture was filtered through a silica plug and the organic solvent was concentrated under reduced pressure. Yields were determined by ^{1}H NMR spectroscopy using an internal standard (CH_2Br_2).

General Procedure D: Reaction Shown in Scheme 2b. In a nitrogen-filled glovebox (in the dark), benzaldehyde (**11**) (15.3 µL; 150 µmol), 4-cyanopyridine (**12**) (10.4 mg; 100 µmol), *i*-Pr_2NEt (26 µL, 150 µmol), photocatalyst (2.0 µmol), and DMSO (1 mL) were successively added to a 4-mL glass vial containing a stir bar. This vial was then capped and placed in the blue LED photoreactor and magnetically stirred. The vial was irradiated while maintained at 25 °C. After 24 h, the reaction mixture was filtered through a silica plug and the organic solvent was concentrated under reduced pressure. Yields were determined by ^{1}H NMR spectroscopy using an internal standard (CH_2Br_2).

General Procedure E: Reaction Shown in Scheme 2c. In the dark in air, anethole (**14**) (0.80 mmol, 120 µL), isoprene {2.40 mmol, 240 µL; isoprene (neat) was passed through a basic alumina plug prior to use} were combined in CH_2Cl_2 (12 mL) with photocatalyst (1.6 µmol) to form a stock solution. 1.5 mL of this stock solution was added to a 4-mL glass vial containing a magnetic stir bar. The vial was then placed in a blue LED photoreactor and magnetically stirred. The vial was irradiated while maintained at 25 °C. After 2 h, the reaction mixture was filtered through a silica plug and the organic solvent was concentrated under reduced pressure. Yields were determined by ^{1}H NMR spectroscopy using an internal standard (CH_2Br_2).

General Procedure F: Reaction Shown in Scheme 2d. In a nitrogen-filled glovebox (in the dark), *trans*-1-(3-phenylallyl)pyrrolidine (*trans*-**16**) (40 mg, 0.21 mmol), *i*-Pr_2NEt (3.5 µL, 20 µmol), photocatalyst (1.5 µmol), and CH_3CN (1.1 mL) were successively added to a 4-mL glass vial containing a stir bar. This vial was then capped and placed in the blue LED photoreactor and magnetically stirred. The vial was irradiated while maintained at 30 °C. After 24 h, the reaction mixture was concentrated under reduced pressure. The ensuing residue was subjected to flash column chromatography (silica gel; 40% EtOAc/hexanes containing 1% Et_3N) to afford the product as a yellow oil. The *E*:*Z* ratio was determined by ^{1}H NMR spectroscopy.

General Procedure G: Reaction Shown in Table 5. In air (in the dark), *N*-phenylmaleimide (**18**) (8.7 mg, 50 µmol), *N*,*N*-dimethyl-*p*-toluidine (15 µL, 100 µmol), and the photocatalyst (1.8 µmol) were successively added to a 4-mL glass vial containing a stir bar. This vial was then capped and placed in the blue LED photoreactor and magnetically stirred. The vial was irradiated while maintained at 25 °C. After 24 h, the reaction mixture was filtered through a silica plug and the organic solvent was concentrated under reduced pressure. Yields were determined by ^{1}H NMR spectroscopy using an internal standard (CH_2Br_2).

X-ray Crystallography. Data for complexes **1**–**5** were collected at 100 K using Cu Kα radiation on a XtaLAB Synergy, Single source HyPix diffractometer. The structures were solved using dual methods with SHELXT-2014, refined using full-matrix least-squares routines against F^2 with SHELXL-2014,[13] and visualized using OLEX2.[14] All non-hydrogen atoms were refined anisotropically. All hydrogen atoms attached to carbon were placed in calculated positions and refined using a riding model with fixed C–H distances of 0.95 Å (sp^2CH). The thermal parameters of hydrogen atoms were estimated as U_{iso}(H) = 1.2U_{eq}(C). CCDC-2106522–2106526 contain the supplementary crystallographic data for complexes **1**–**5**. The data can be obtained free of charge from The Cambridge Crystallographic Data Centre via http://www.ccdc.cam.ac.uk/data_request/cif.

Photophysical Measurements. Absorption spectra were recorded at room temperature on a PerkinElmer Lambda 35 UV/Vis spectrometer. Uncorrected steady-state emission and excitation spectra were recorded using an Edinburgh FLSP980-

stm spectrometer equipped with a 450 W xenon arc lamp, double excitation and emission monochromators, a Peltier-cooled Hamamatsu R928P photo- multiplier (185–850 nm). Emission and excitation spectra were corrected for source intensity (lamp and grating) and emission spectral response (detector and grating) by a calibration curve supplied with the instrument. Emission lifetimes (τ) were determined using the single photon counting technique (TCSPC) with a pulsed picosecond LED (EPL 375). Quantum yields (Φ) were calculated according to the optically dilute method reported by Demas and Crosby against the reference $[Ru(bpy)_3]Cl_2$($\Phi = 0.028$, air equilibrated).[15,16] Experimental uncertainties are estimated to be ±8% for lifetime determinations, ±20% for quantum yields, and ±2 nm and ±5 nm for absorption and excitation/emission peaks, respectively. All solvents used in the preparation of the solutions for the photophysical investigations were of spectrometric grade.

Electrochemical Measurements. Cyclic voltammetry was performed at room temperature using a Metrohm Autolab PGSTAT101 and data acquired with Metrohm Autolab, Nova 2.0 software. Samples were prepared in a nitrogen-filled glovebox and sparged with argon before measurements were recorded. Experiments were performed in dry, degassed DMF (10 mM), NBu_4BF_4 (0.1 M) supporting electrolyte (scan rate of 100 mV/s), with a CH Instruments glassy carbon working electrode, Pt wire counter electrode, and Ag wire reference electrode (Ag/Ag^+). Ferrocene (Fc) (10 mM) was added as an internal standard in various experiments.

Computational Studies. All DFT and TD-DFT calculations were performed with the Gaussian 16 software package.[17] Ground state geometries were optimized in solution at the wB97XD[18]/Def2-TZVP[19] level of theory with SMD solvent model[20], and frequencies were also calculated at this level. Geometries were verified as local minima (possessing no imaginary frequencies), and geometries were shown to reproduce the corresponding crystal structures to within 0.02Å (bonds) and 2° (angles) (Table S1). The UV-VIS absorption spectra were simulated via TD-DFT calculations at the same level and used to assign the experimental data.

RESULTS AND DISCUSSION

Synthesis and Spectroscopic Characterization of Complexes. Complexes **1**–**5** were prepared by applying the procedure employed for the synthesis of analogous complex **F**.[8a] Specifically, imidazolium **6** was heated in refluxing toluene under argon to afford the corresponding metal carbonyl (Scheme 1). After work-up and isolation, complexes **1**–**4** were obtained as air-stable solids in moderate to good yields. Complexes **1**–**4** have the general form $[ML(CO)_3X]$, where X = CO for **1**–**3** and X = Br for **4**; L = 1-phenyl-3-(2-pyridyl)imidazolium. Iron complex **5**, $[FeL(CO)_3]$, proved to be an air-sensitive solid and its inherent paramagnetic nature prevented NMR spectroscopic characterisation.[21] ^{1}H NMR spectroscopic analysis of complexes **1**–**4** was consistent with the absence of the imidazolium NC*H*N hydrogen signal, which supported carbene formation. IR spectroscopy also indicated the presence of metal–carbonyl bonds in each case. Indeed, complexes **1**–**5** all displayed three strong IR signals that were consistent with the three inequivalent CO environments. These observations were in agreement with their expected respective geometries and their ^{13}C NMR spectroscopic data. The CO IR signals for complexes **1**–**4** are similar and consistent with closely related analogous NHC-ligated Group 7 and 8 metal carbonyl complexes.[22]

Scheme 1. Synthesis of complexes 1–5 from imidazolium 6.

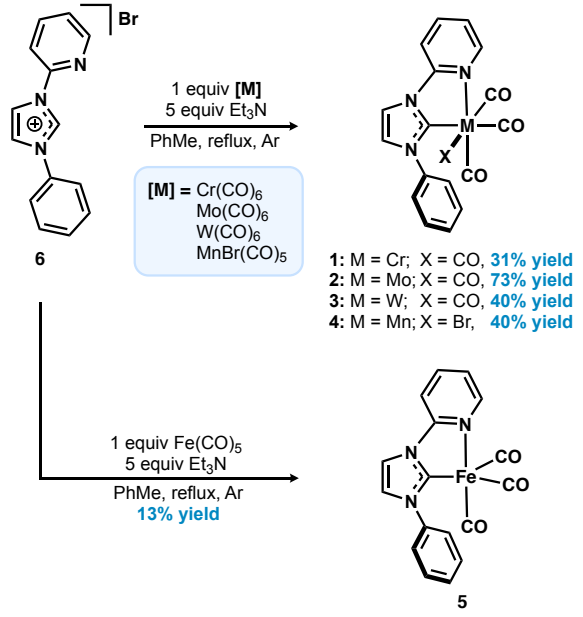

X-Ray Crystallographic Studies. In each case, crystals suitable for analysis by X-ray diffraction of complexes **1**–**5** were grown by slow evaporation of CH_3CN or toluene solutions. Selected bond lengths and angles are summarized in Figure 2.

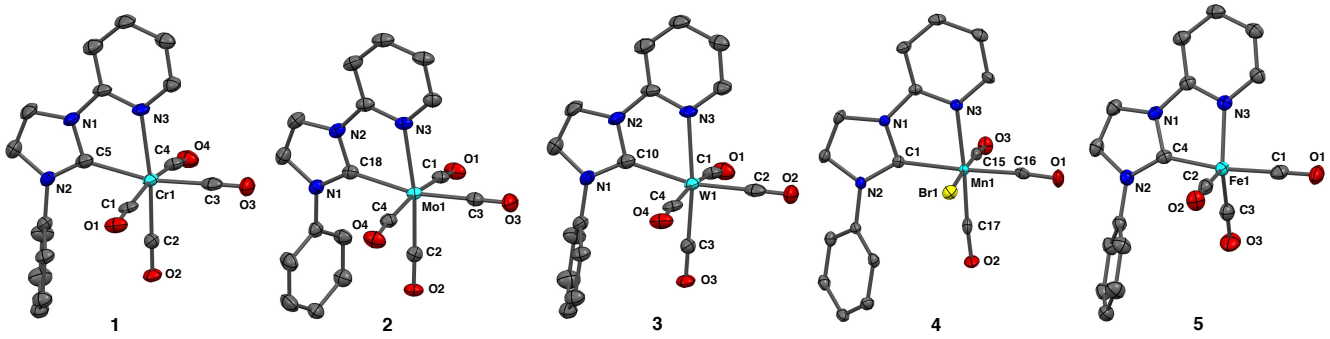

Figure 2. Structural representations of complexes **1**–**5** with thermal ellipsoids drawn at the 50% probability level and hydrogen atoms omitted for clarity. Complex **1**, selected bond lengths (Å) and angles (°): Cr1–C1,C2,C3,C4,C5,N3 1.900(2), 1.849(3), 1.859(3), 1.890(2), 2.043(2), 2.149(2), C1–O1 1.142(3), C2–O2 1.161(3), C3–O3 1.161(4), C4–O4 1.146(3), C5–Cr1–N3 75.90(9), C5–Cr1–C2 98.99(10), N3–Cr1–C3

92.50(9). Complex **2**: Mo1–C1,C2,C3,C4,C18,N3 2.046(2), 1.978(2), 2.003(3), 2.031(3), 2.176(3), 2.279(2), C1–O1 1.136(3), C2–O2 1.151(3), C3–O3 1.153(3), C4–O4 1.147(3), C18–Mo1–N3 72.15(8), C18–Mo1–C2 99.93(9), N3–Mo1–C3 95.59(8). Complex **3**: W1–C1,C2,C3,C4,C10,N3 2.032(5), 1.974(5), 2.022(6), 2.025(5), 2.177(5), 2.263(4), C1–O1 1.153(5), C2–O2 1.157(6), C3–O3 1.132(6), C4–O4 1.153(6), C10–W1–N3 72.08(16), C10–W1–C3 100.19(18), N3–W1–C2 94.54(16). Complex **4**: Mn1–C1,C15,C16,C17,N3 2.026(3), 1.803(4), 1.831(4), 1.805(4), 2.087(3), Mn1–Br1 2.5043(6), C15–O3 1.146(5), C16–O1 1.148(5), C17–O2 1.149(5), C1–Mn1–N3 78.31(12), C1–Mn1–C17 98.40(14), N3–Mn1–C16 95.43(13). Complex **5**: Fe1–C1,C2,C3,C4,N3 1.781(2), 1.770(2), 1.762(2), 1.9245 (19), C1–O1 1.153(3), C2–O2 1.159(3), C3–O3 1.161(3), C4–Fe1–N3 79.59(7), N3–Fe1–C3 134.42(8), N3–Fe1–C2 112.44(8), N3–Fe1–C1 92.10(8).

Table 1. Comparison of M–CO and C–O bond lengths (Å) *trans* to NHC and pyridyl for complexes 1–5.

	Cr **1**	Mo **2**	W **3**	Mn **4**	Fe **5**
M–CO(*trans* NHC)	1.859(3)	2.003(3)	1.974(5)	1.831(4)	1.781(2)
M–CO(*trans* pyridyl)	1.848(2)	1.978(2)	2.022(6)	1.805(4)	1.770(2), 1.762(2)
C–O(*trans* NHC)	1.161(4)	1.153(3)	1.157(6)	1.148(5)	1.153(3)
C–O(*trans* pyridyl)	1.161(3)	1.151(3)	1.132(6)	1.149(5)	1.159(3), 1.161(3)

Complexes **1**–**4** are isostructural featuring slightly distorted octahedral metal coordination geometries owing to the chelated NHC ligand, while complex **5** adopted a trigonal bipyramidal metal coordination geometry. The metal–carbonyl bonds *trans* to the pyridyl nitrogen donor atoms are slightly shorter when compared to the metal–carbonyl bonds *trans* to the NHC carbons (Table 1). This is consistent with the strong □-donor and *trans*-influencing capabilities of NHCs when compared to nitrogen donor atoms.[23] In addition, the strong donor capacity of the NHC moiety can be observed in the elongated C–O bond distances for *trans*-to-NHC CO ligands as a result of □-backbonding (Table 1). This is also seen as a shift in the IR stretch of the relevant CO to a lower wavenumber. Interestingly, this trend is most pronounced moving from complex **1** through to **3** (i.e., down group 7) and less prominent in manganese complex **4**. This trend is also observed when comparing manganese complex **4** to rhenium analogue **F**. The C–O bond length of the CO ligand *trans*-to-NHC in **F** is 1.141(4) Å while the equivalent bond in the CO ligand *trans*-to-pyridyl is slightly longer at 1.149(4) Å.[8a] The metal coordination geometry of iron complex **5** does not permit as direct a comparison, however, the average Fe–CO bond distances *trans* to the pyridyl moiety are also slightly shorter than those *trans* to the NHC carbon.

Photophysical Studies. A summary of the relevant photophysical data can be found in Table 2. Due to its pronounced air-sensitivity, iron complex **5** was not investigated. Molecules **1**–**4** exhibit absorption spectra with comparable features, which is expected given their structural similarities (Figure 3). High energy bands are present between 200 and 300 nm, while a red-shifted band appears above 300 nm, with maxima around 390–401 nm. Interestingly, the corresponding simulated spectra for complexes **1**–**4** in acetonitrile are qualitatively different, with this secondary peak considerably blue-shifted compared with experiment (Figure 3). The primary peaks are largely aligned in the measured and computed spectra, although they are somewhat obscured in the latter by solvent peaks below 250 nm.[24]

Table 2. Photophysical data for complexes 1–4. Measurements were performed in diluted CH_3CN solutions at room temperature.

Complex	λ_{abs} [nm] (10^{-4} ε [M^{-1} cm^{-1}])	λ_{em} (nm)	τ (ns)	Φ (%)
Cr **1**	270 (1.88), 401 (0.488)	–	–	–
Mo **2**	259 (2.82), 390 (0.609)	681	–	–
W **3**	253 (3.59), 396 (0.589)	670	10.8[a] 13.0[b]	0.06[a] 0.08[b]
Mn **4**	268 (1.24), 399 (0.233)	–	–	–

[a]Aerated solution. [b]Air-free solution.

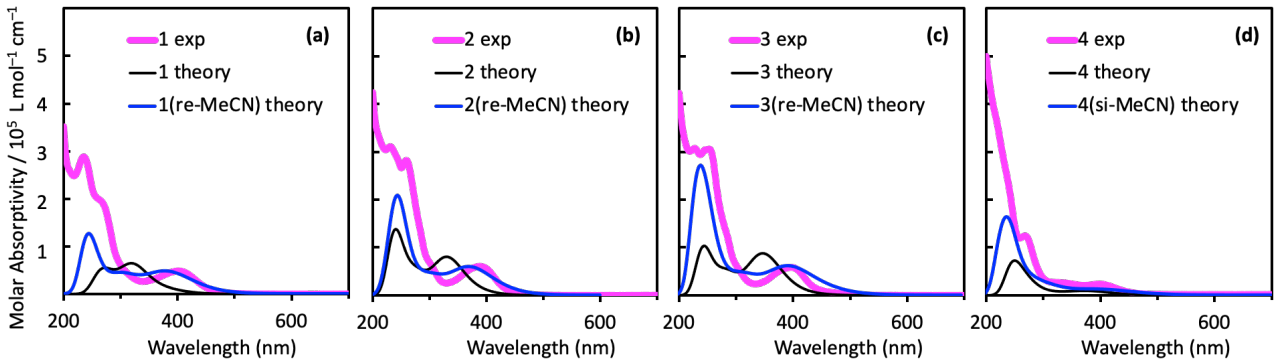

Figure 3. Experimental and wB97XD/Def2-TZVP simulated absorption spectra of complexes **1** (a), **2** (b), **3** (c), and **4** (d) in CH_3CN solutions. Simulated spectra are shown for the original complexes and for those in which the re-CO is substituted with CH_3CN, except for Mn **4** where the re-position is a Br and so substitution at the si-position is shown instead. Simulated spectra for the decarbonylated complexes and substituted complexes at all positions are shown in the Supporting Information (Figures S10–S13).

Given this blue-shifting of theory versus experiment, we suspected that, upon exposure to UV light, decarbonylation might occur. Previous studies have demonstrated the photoreactivity of analogous complexes upon excitation to the lowest MLCT manifold,[25,26] with photoinduced decarbonylation occurring, as evidenced by a red-shift of the MLCT band.[8a,25] In control experiments, CH_3CN and CH_2Cl_2 solutions of complexes **1**–**4** were found to be stable for prolonged times while being kept in the dark (> 24 h). However, when the solutions were exposed to either laboratory ambient light or blue light (467 nm), changes in the respective absorption spectra measured every hour became evident. In general, a reduction of the MLCT band is observed.

Using TD-DFT, we simulated the spectra for the decarbonylated complexes (middle panels of Figures S25–S28, Supporting Information). However, these were also inconsistent with experiment. Interestingly, the secondary peak in the respective simulated spectra is now considerably red-shifted, rather than blue-shifted, when compared with experiment. Next, we considered the respective complexes that would result from decarbonylation and acetonitrile binding to the ensuing vacant coordination site (right panels of Figures S25–S28, Supporting Information). While the overall substitution of CO for CH_3CN is endergonic in the ground state, photoinduced decarbonylation is irreversible (as CO gas leaves the solution), and, depending on the position, the subsequent association of CH_3CN to the decarbonylated complexes is thermodynamically favorable (Table S2, Supporting Information). TD-DFT simulated spectra for the substituted compounds showed good qualitative agreement with experiment. There are minor differences amongst them, depending on which position the CH_3CN occupies but the general features are similar. For simplicity the spectra resulting from substitution at the re-position for **1**–**3** are included in Figure 3, as this position was consistently found to be the most energetically favorable site for decarbonylation (Table S2, Supporting Information). For manganese complex **4**, decarbonylation at the si-position is shown instead, as a Br occupies the re-position in this case.

From previously reported data,[8a,25,27] the respective lower energy bands are attributed to metal-to-ligand charge transfer transitions (MLCT), while the respective intense higher energy bands originate from ligand centered (LC) π–π* transitions. Our TD-DFT calculations support these assignments, and show the peaks are assigned to MLCT for the lower energy bands and to LC for the intense higher bands (Figure 4).

The IR spectrum of tungsten complex **3** in CH_3CN displays 3 signals (2004, 1886 and 1833 cm^{-1}) consistent with three inequivalent CO environments. After UV irradiation of molecule **3** in degassed, anhydrous CH_3CN for 3 h, the IR band at 2004 cm^{-1} is significantly diminished, the signal at 1886 cm^{-1} has shifted to 1899 cm^{-1}, and the signal at 1833 cm^{-1} has shifted to 1785 cm^{-1} (Figure S14, Supporting Information). The ^1H NMR spectrum of this irradiated sample of complex **3** also revealed new resonances in the aromatic region (Figure S15, Supporting Information). These observations are consistent with photodissociation of a CO ligand from complex **3** upon irradiation.

Upon excitation at 390 nm in fluid CH_3CN solution at room temperature, complexes **1** and **4** displayed no emission. On the other hand, complexes **2** and **3** were weakly luminescent, featuring a broad and structureless emission band ranging from 600–800 nm and maxima appearing around 670–680 nm. These emission profiles, typical of radiative decay from ^{3}MLCT excited states, are similar to previously reported $[W(CO)_4(diim)]$ complexes (where diim represents a diimine-type ligand).[25,27] The results were analogous when excitation occurred in CH_2Cl_2 solutions, indicating a lack of solvatochromism. The lifetime and quantum yield of **3** was recorded at 10.8 ns and 0.06% in an aerated solution, increasing to 13.0 ns and 0.08% in an air-free environment (Table 2). These values appear to be somewhat lower than a few previously reported $[W(CO)_4(diim)]$ complexes,[25,27] but still in agreement with relatively weak luminescence properties.

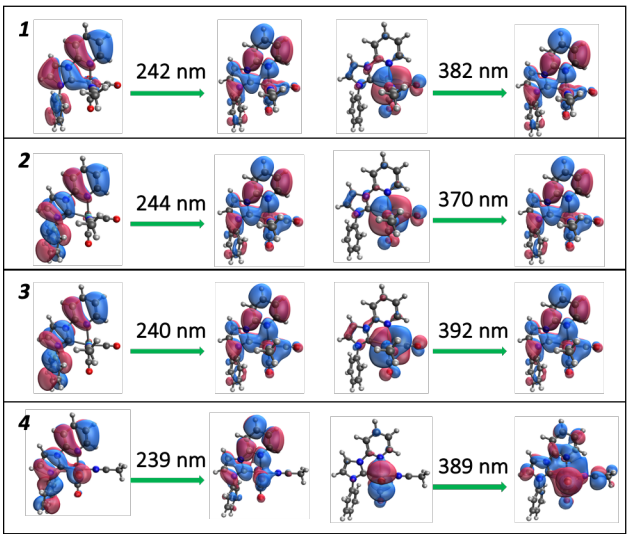

Figure 4. Orbital transitions associated with the two primary peaks in the absorption spectra of the complexes in which the re (**1**–**3**) or si (**4**) CO ligand is substituted with CH_3CN.

Table 3. Electrochemical data for complexes 1–4 in degassed DMF solutions at ambient temperature. All potentials are given in volts (V) versus Ag/Ag^+.

complex	redox potentials
Cr **1**	+0.93 V (irreversible) +1.53 V (irreversible)
Mo **2**	+1.06 V (irreversible)
W **3**	+1.07 V (irreversible)
Mn **4**	–0.86 V (reversible) +1.43 V (quasi-reversible) –1.23 V; –1.85 V (irreversible)

Electrochemical Studies. The electrochemical characterization of **1**–**4** was performed in DMF (Table 3).[28] Chromium complex **1** displayed irreversible oxidation behavior ($E_{½}$ = +0.93 V and +1.53 V) (Figure 5). Molybdenum and tungsten analogues

2 and **3** showed irreversible oxidation steps ($E_{½}$ = +1.06 V and +1.07 V), respectively (See Supporting Information). Consistent with electrochemical studies on related complexes,[29] this behavior may be attributed to the higher lability of the molybdenum/tungsten M–CO bonds upon oxidation in comparison to the equivalent chromium M–CO bond. Interestingly, manganese complex **4** exhibited reversible oxidation and reduction behavior ($E_{½}$ = +1.43 V and –0.86 V) (Figure 5). In addition, molecule **4** also displayed irreversible reductions ($E_{½}$ = –1.23 and –1.85 V).[30] The reduction behavior of complex **4** is consistent with similar NHC-ligated manganese carbonyl complexes.[22a]

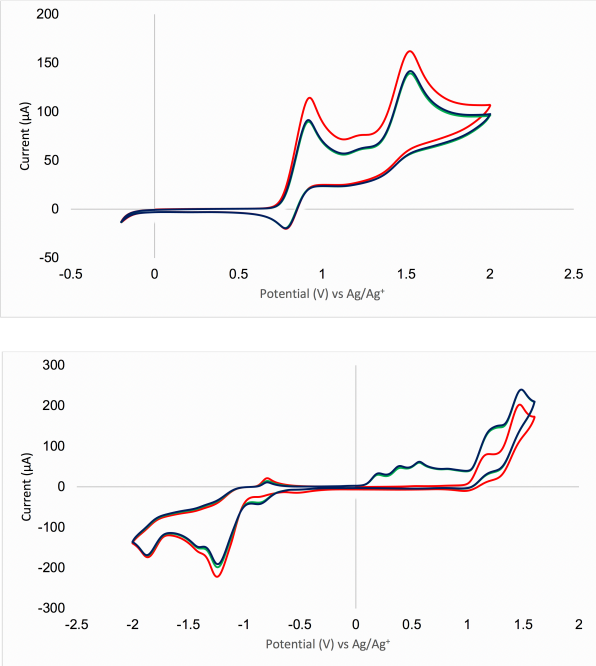

Figure 5. Cyclic voltammogram of Cr complex **1** (10 mM) in DMF (top); and Mn complex **4** (10 mM) in DMF (bottom); NBu_4PF_6 (0.1 M) supporting electrolyte.

Photocatalysis. We selected 6 different reactions from which to comprehensively evaluate the capacity for complexes **1**–**4** to facilitate photoinduced synthetic reactions. In each case, this reactivity was benchmarked against an established ruthenium/iridium photocatalyst or an organic dye. By design, we selected a broad range of transformations that would allow us to explore the ability of these complexes to promote either the reductive or oxidative functionalization of organic substrates via photoredox, in addition to photoinduced energy transfer processes. We anticipated this approach would reveal more pertinent findings concerning the scope and viability of complexes **1**–**4** beyond the information provided by their aforementioned intrinsic photophysical and electrochemical properties.

The reductive functionalization of organic molecules is a fundamental application of photoredox catalysis.[1] Atom-transfer radical addition (ATRA) reactions, in which the reductive cleavage of a bond within a transfer agent leads to the vicinal addition of reactive intermediates across a □-bond, represent one of the most common types of photoredox-catalyzed transformations. With this in mind, we investigated the ability of complexes **1**–**4** to mediate the chloro-N-tosylation of styrene **7** (Table 4).[31] Pleasingly, manganese and chromium species **4** and **1** afforded product **8** in good yields and compared well to prototypical photoredox catalyst $[Ru(bpy)_3]^{2+}$. In comparison, molybdenum and tungsten catalysts **2** and **3** were less efficient.

Table 4. Investigation of photoredox-catalyzed ATRA reactions: vicinal chloro-N-tosylation.

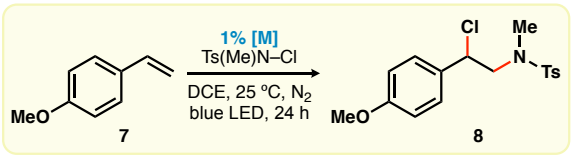

7 8

entry	[M]	conversion (%)[a]	yield (%)[a]
1	Cr **1**	100	86
2	Mo **2**	98	71
3	W **3**	91	32
4	Mn **4**	100	94
5	$[Ru(bpy)_3](PF_6)_2$	100	>99
6	–	84	17

Reactions performed employing 100 □mol **7**; bpy = 2,2'-bipyridyl. [a]Conversion of **7** and yield of **8** determined by ^{1}H NMR spectroscopy with the aid of a calibrated internal standard (average of 2 experiments). Product **8** was formed in trace yield in respective experiments performed in the presence of catalysts in the dark.

Scheme 2. Investigating the scope of complexes 1–4 in particularly challenging photoredox reactions: (a) reductive decarboxylation, (b) reductive coupling, (c) formal [4+2]-cycloaddition (oxidative functionalization); and (d) *trans*-/*cis*-photoisomerization (energy transfer).

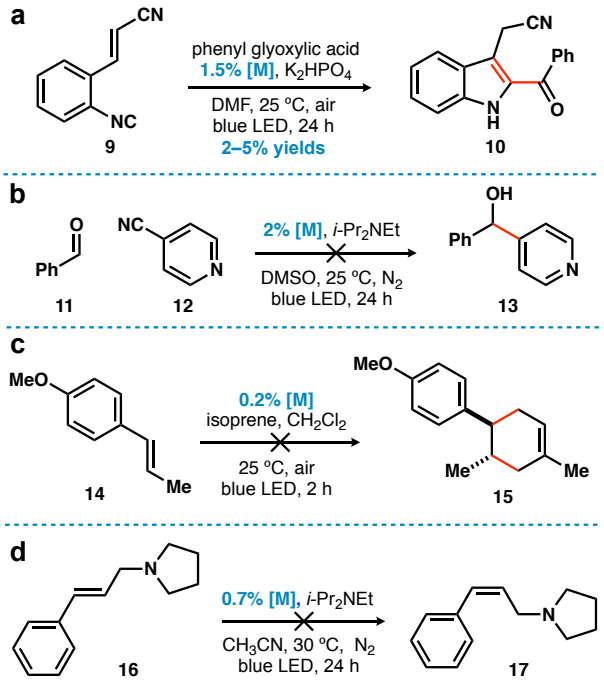

Our electrochemical studies (Table 3) suggested that complexes **1**–**4** were unlikely to facilitate more challenging transformations that require highly reducing catalysts. In such processes, $[Ru(bpy)_3]^{2+}$ is not suitable and highly reducing iridium photoredox catalysts are necessary. To this end, we explored the more difficult reductive decarboxylation and reductive coupling processes shown in Schemes 2a and 2b.[32,33] Consistent with our

expectations, these experiments confirmed that complexes **1**–**4** could not promote these reactions effectively (Schemes 2a and 2b; Schemes S1 and S2, Supporting Information).

The oxidative functionalization organic molecules under mild conditions is another important application of photoredox catalysis.[1] One important mode of reactivity within this manifold is the oxidation of □-amino C–H bonds leading to carbon-centered □-amino radicals (or iminium species) that allow for the efficient derivatization of tertiary amines. With this in mind, we investigated the capacity of complexes **1**–**4** to promote the Povarov-type reaction between *N*-phenylmaleimide (**14**) and *N*,*N*-dimethyl-*p*-anisidine (Table 5).[34] Complexes **1**–**4** were not particularly effective in facilitating the oxidative functionalization of *N*,*N*-dimethyl-*p*-anisidine, with molybdenum complex **2** affording the best results in this manifold. In all cases, increasing the catalyst loading did not improve these results.

Table 5. Investigation of a photoredox-catalyzed oxidative functionalization: Povarov-type reaction.

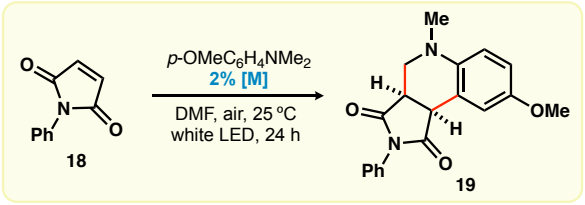

entry	[M]	conversion (%)[a]	yield (%)[a]
1	Cr **1**	86	20
2	Mo **2**	88	30
3	W **3**	84	15
4	Mn **4**	84	3
5	$[Ru(bpy)_3](PF_6)_2$	86	54
6	–	86	5

Reactions performed employing 50 □mol **18**. [a]Conversion of **18** and yield of **19** determined by ^{1}H NMR spectroscopy with the aid of a calibrated internal standard (average of 2 experiments).

Our electrochemical studies (Table 3) and the findings shown in Table 5 suggested that complexes **1**–**4** were unlikely to facilitate more challenging transformations that require highly oxidizing catalysts. The so-called radical cation Diels–Alder reaction, in which highly oxidizing organic photoredox catalysts or more oxidizing derivatives of $[Ru(bpy)_3]^{2+}$ activate anethole (**14**) (and related compounds), is one such example (Scheme 2c).[35] These experiments confirmed that complexes **1**–**4** could not promote these more difficult reactions effectively (Scheme 2c; Scheme S3, Supporting Information).

Photoredox catalysis relates to photoinduced transformations involving single-electron transfer processes that are facilitated by a redox-active catalyst in its photoexcited state.[36] In contrast, energy transfer photocatalysis concerns, "*the photophysical process in which an excited state of one molecular entity (the donor) is deactivated to a lower-lying state by transferring energy to a second molecular entity (the acceptor), which is thereby raised to a higher energy state*".[37] Synthetic applications of energy transfer photocatalysis are not as well developed as photoredox catalysis.[36] We identified the reported photocatalyzed *trans*-/*cis*-isomerization reaction shown in Scheme 2d as an excellent system from which we could evaluate the viability of complexes **1**–**4** to facilitate photoinduced energy transfer catalysis.[38] Unfortunately, our experiments indicated that these molecules could not promote this *trans*-/*cis*-isomerization transformation (Scheme 2d; Scheme S4, Supporting Information).

CONCLUSIONS

A number of structurally-related chromium, molybdenum, tungsten, manganese, and iron complexes **1**–**5** have been synthesized. We studied their respective structures in the solid state and investigated their spectroscopic, photophysical, and electrochemical properties where possible. Single crystal X-ray crystallographic analysis revealed slight systematic shortening in metal–carbonyl bond lengths *trans* to NHC carbon for transition metal complexes in the same group {i.e., **1**–**3** (group 6**)**; **4** and **F** (group 7**)**}. This is consistent with the strong s-donor and *trans*-influencing capability of the NHC ligand in comparison to nitrogen donor atom of the pyridyl moiety. Our photophysical studies reveal that decarbonylation occurs upon exposure to UV light, with the CO ligand being replaced with a labile CH_3CN solvent molecule. In cyclic voltammetry experiments, chromium complex **1** displayed irreversible oxidation behavior, in addition to a quasi-reversible oxidation step. Molybdenum and tungsten analogues **2** and **3** showed irreversible oxidation steps, while manganese species **4** exhibited reversible oxidation and reduction behavior (in addition to irreversible reductions).

We comprehensively evaluated the capacity of complexes **1**–**4** to serve as photoredox catalysts. These complexes were not capable of efficiently promoting a Povarov reaction via the oxidative functionalization of *N*,*N*-dimethyl-*p*-anisidine, with the best results provided by molybdenum catalyst **2** (30% product yield). However, our findings demonstrate that molecules **1**, **2**, and, **4** can efficiently facilitate chloro-*N*-tosylation ATRA processes, likely via their respective reductive quenching cycles. When considered within the context of their photolability, these types of complexes may allow for the development of photoinduced ATRA reactions that involve less conventional inner-sphere electron transfer pathways, such as the transformations more usually associated with copper photocatalysts.[39] This will be the subject of future work in our laboratory.

ASSOCIATED CONTENT

Supporting Information

Additional experimental information and compound characterization data. This material is available free of charge via the Internet at http://pubs.acs.org.

AUTHOR INFORMATION

Corresponding Author

*E-mail for M.L.C.: michelle.coote@anu.edu.au;
*E-mail for C.C.H.: curtis.ho@utas.edu.au
*E-mail for A.C.B.: alex.bissember@utas.edu.au

Notes

The authors declare no competing financial interest.

ACKNOWLEDGMENTS

We gratefully acknowledge the University of Tasmania (UTAS) School of Natural Sciences – Chemistry and an Australian Research Council (ARC) Discovery Project Grant (DP210100025) for funding, and the UTAS Central Science Laboratory for providing access to NMR spectroscopy services. S.A.M.'s contributions were supported by an ARC Future Fellowship (FT200100243). R.O.F.'s contributions were supported by an ARC Discovery Early Career

Research Award (DE180100112). M.L.C. gratefully acknowledges an ARC Laureate Fellowship (FL170100041) and generous allocations of supercomputing time on the National Facility of the Australian National Computational Infrastructure. A.C.B.'s contributions were supported by an ARC Future Fellowship (FT200100049).

REFERENCES

(1) For selected reviews on applications of photoredox catalysis in organic synthesis, see: (a) Prier, C. K.; Rankic, D. A.; MacMillan, D. W. C. Visible Light Photoredox Catalysis with Transition Metal Complexes: Applications in Organic Synthesis. *Chem. Rev*. **2013**, *113*, 5322–5363; (b) Koike, T.; Akita, M. Visible-Light-Induced Photoredox Catalysis: An Easy Access to Green Radical Chemistry. *Synlett* **2013**, *24*, 2492–2505; (c) Nicholls, T. P.; Leonori, D.; Bissember, A. C. Applications of visible light photoredox catalysis to the synthesis of natural products and related compounds. *Nat. Prod. Rep*. **2016**, *33*, 1248–1254. (d) Shaw, M. H.; Twilton, J.; MacMillan, D. W. C. Photoredox Catalysis in Organic Chemistry. *J. Org. Chem.* **2016**, *81*, 6898–6926; (e) Marzo, L.; Pagire, S. K.; Reiser, O.; König, B. Visible-Light Photocatalysis: Does It Make a Difference in Organic Synthesis? *Angew. Chem., Int. Ed.* **2018**, *57*, 10034–10072.

(2) For selected reviews on the development of earth abundant and/or less established transition-metal-based photoredox catalysts, see: (a) Larsen C. B.; Wenger, O. S. Photoredox Catalysis with Metal Complexes Made from Earth-Abundant Elements. *Chem. – Eur. J.* **2018**, *24*, 2039–2058. (b) Wenger, O. S. Photoactive Complexes with Earth-Abundant Metals. *J. Am. Chem. Soc*. **2018**, *140*, 13522–13533. (c) Hockin, B. M.; Li, C.; Robertson N.; Zysman-Colman, E. Photoredox catalysts based on earth-abundant metal complexes. *Catal. Sci. Technol*. **2019**, *9*, 889–915. (d) Glaser, F.; Wenger, O. S. Recent progress in the development of transition-metal based photoredox catalysts. *Coord Chem. Rev*. **2020**, *405*, 213129.

(3) For examples of chromium-based photoredox catalysts in synthesis, see: (a) Stevenson, S. M.; Shores, M. P.; Ferreira, E. M. Photooxidizing Chromium Catalysts for Promoting Radical Cation Cycloadditions. *Angew. Chem., Int. Ed*. **2015**, *54*, 6506−6510. (b) Higgins, R. F.; Fatur, S. M.; Shepard, S. G.; Stevenson, S. M.; Boston, D. J.; Ferreira, E. M.; Damrauer, N. H.; Rappe, A. K.; Shores, M. P. Uncovering the Roles of Oxygen in Cr(III) Photoredox Catalysis. *J. Am. Chem. Soc.* **2016**, *138*, 5451−5464. (c) Stevenson, S. M.; Higgins, R. F.; Shores, M. P.; Ferreira, E. M. Chromium photocatalysis: accessing structural complements to Diels–Alder adducts with electron-deficient dienophiles. *Chem. Sci*. **2017**, *8*, 654−660. (d) Sarabia, F. J.; Ferreira, E. M. Radical Cation Cyclopropanations via Chromium Photooxidative Catalysis. *Org. Lett*. **2017**, *19*, 2865−2868. (e) Büldt, L. A.; Wenger, O. S. Chromium complexes for luminescence, solar cells, photoredox catalysis, upconversion, and phototriggered NO release. *Chem. Sci*. **2017**, *8*, 7359−7367. (f) Otto, S.; Nauth, A. M.; Ermilov, E.; Scholz, N.; Friedrich, A.; Resch-Genger, U.; Lochbrunner, S.; Opatz, T.; Heinze, K. Photo-Chromium: Sensitizer for Visible-Light-Induced Oxidative C–H Bond Functionalization–Electron or Energy Transfer? *ChemPhotoChem* **2017**, *1*, 344–349. (g) Sarabia, F. J.; Li, Q.; Ferreira, E. M. Cyclopentene Annulations of Alkene Radical Cations with Vinyl Diazo Species Using Photocatalysis. *Angew. Chem., Int. Ed*. **2018**, *57*, 11015–11019. (h) Higgins, R. F.; Fatur, S. M.; Damrauer, N. H.; Ferreira, E. M.; Rappe, A. K.; Shores, M. P. Detection of an Energy-Transfer Pathway in Cr-Photoredox Catalysis. *ACS Catal*. **2018**, *8*, 9216−9225.

(4) For examples of molybdenum-based photoredox catalysts in synthesis, see: (a) Büldt, L. A.; Guo, X.; Prescimone, A.; Wenger, O. S. A Molybdenum(0) Isocyanide Analogue of Ru(2,2'-Bipyridine)$_3^{2+}$: A Strong Reductant for Photoredox Catalysis. *Angew. Chem., Int. Ed*. **2016**, *55*, 11247–11250. (b) Bilger, J. B.; Kerzig, C.; Larsen C. B.; Wenger, O. S. A Photorobust Mo(0) Complex Mimicking [Os(2,2′-bipyridine)3]$^{2+}$ and Its Application in Red-to-Blue Upconversion. *J. Am. Chem. Soc*. **2021**, *143*, 1651–1663.

(5) For examples of tungsten-based photoredox catalysts in synthesis, see: Yeung, K.-T.; To, W.-P.; Sun, C.; Cheng, G.; Ma, C.; Ming Tong, G. S. M.; Yang, C.; Che, C.-M. Luminescent Tungsten(VI) Complexes: Photophysics and Applicability to Organic Light-Emitting Diodes and Photocatalysis. *Angew. Chem., Int. Ed*. **2017**, *56*, 133 –137.

(6) For examples of manganese-based photoredox catalysts in synthesis, see: (a) Nuhant, P.; Oderinde, M. S.; Genovino, J.; Juneau, A.; Gagné, Y.; Allais, C.; Chinigo, G. M.; Choi, C.; Sach, N. W.; Bernier, L.; Fobian, Y. M.; Bundesmann, M. W.; Khunte, B.; Frenette, M.; O. Fadeyi, O. O. Visible-Light-Initiated Manganese Catalysis for C–H Alkylation of Heteroarenes: Applications and Mechanistic Studies. *Angew. Chem., Int. Ed*. **2017**, *56*, 15309–15313. (b) Dong, J.; Wang, X.; Wang, Z.; Song, H.; Liu, Y.; Wang, Q. Visible-light-initiated manganese-catalyzed Giese addition of unactivated alkyl iodides to electron-poor olefins. *Chem. Commun.* **2019**, *55*, 11707–11710. (c) Long, W.; Lian, P.; Li J.; Wan, X. Mn-Catalysed photoredox hydroxytrifluoromethylation of aliphatic alkenes using CF_3SO_2Na. *Org. Biomol. Chem*. **2020**, *18*, 6483–6486. (d) Wang, X.; Dong, J.; Li, Y.; Liu, Y.; Wang, Q. Visible-Light-Mediated Manganese-Catalyzed Allylation Reactions of Unactivated Alkyl Iodides. *J. Org. Chem*. **2020**, *85*, 7459−7467. (e) Herr, P.; Kerzig, C.; Larsen, C. B.; Häussinger, D.; Wenger, O. S. Manganese(I) complexes with metal-to-ligand charge transfer luminescence and photoreactivity. *Nat. Chem*. **2021**, doi:10.1038/s41557-021-00744-9.

(7) For examples of iron-based photoredox catalysts in synthesis, see: (a) Gualandi, A.; Marchini, M.; Mengozzi, L.; Natali, M.; Lucarini, M.; Ceroni, P.; Cozzi, P. G. Organocatalytic Enantioselective Alkylation of Aldehydes with $[Fe(bpy)_3]Br_2$ Catalyst and Visible Light. *ACS Catal*. **2015**, *5*, 5927−5931. (b) Parisien-Collette, S.; Hernandez-Perez, A. C.; Collins, S. K. Photochemical Synthesis of Carbazoles Using an $[Fe(phen)_3](NTf_2)_2/O_2$ Catalyst System: Catalysis toward Sustainability. *Org. Lett*. **2016**, *18*, 4994−4997.

(8) (a) Vaughan, J. G.; Reid, B. L.; Ramchandani, S.; Wright, P. J.; Muzzioli, S.; Skelton, B. W.; Raiteri, P.; Brown, D. H.; Stagni, S.; Massi, M. The photochemistry of rhenium(i) tricarbonyl N-heterocyclic carbene complexes. *Dalton Trans*. **2013**, *42*, 14100–14114. (b) Vaughan, J. G.; Reid, B. L.; Wright, P. J.; Ramchandani, S.; Skelton, B. W.; Raiteri, P.; Muzzioli, S.; Brown, D. H.; Stagni, S.; Massi, M. Photophysical and Photochemical Trends in Tricarbonyl Rhenium(I) N-Heterocyclic Carbene Complexes. *Inorg. Chem*. **2014**, *53*, 3629–3641.

(9) Nicholls, T. P.; Burt, L. K.; Simpson, P. V.; Massi, M.; Bissember, A. C. Tricarbonyl rhenium(I) tetrazolato and N-heterocyclic carbene complexes: versatile visible-light-mediated photoredox catalysts. *Dalton Trans.* **2019**, *48*, 12749–12754.

(10) For a selected reports of relevant photoactive transition metal carbonyl complexes and their reactions, see for example: (a) Wrighton, M., Photochemistry of metal carbonyls. *Chem. Rev.* **1974,** *74,* 401–430. (b) Rausch, M. D.; Gismondi, T. E.; Alt, H. G.; Schwäbzle, J. A., The Photochemically-Induced Degradation of $(\eta^5\text{-}C_5H_5)M(CO)_3CH_3$ Complexes (M = Cr, Mo, W). *Z. Naturforsch. B* **1977,** *32,* 998–1000. (c) Gismondi, T. E.; Rausch, M. D., Photo-induced degradation reactions of some alkyl- and aryl-carbonyl derivatives of manganese, molybdenum and tungsten. *J. Organomet. Chem.* **1985,** *284*, 59–71. (d) Naman, S. A.; Jassim, A. H.; Alias, M. F., Photodecomposition of molybdenum(II) and tungsten(II) carbonyl complexes with triazole, benz-imidazole, and oxadiazole acetylinic derivatives. *J. Photochem. Photobiol. A* **2002,** *150*, 41–48. (e) Ye, Q.; Wu, Q.; Zhao, H.; Song, Y.-M.; Xue, X.; Xiong, R.-G.; Pang, S.-M.; Lee, G.-H., Two noncentrosymmetric complexes: [W(CO)4(bipy)] and [W(CO)4(phen)](bipy=2,2′-bipyridine, phen=1,10-phenanthroline) obtained through solvothermal synthesis and their optical properties. *J. Organomet. Chem.* **2005,** *690,* 286–290. (f) Lee, J. J.; Yap, C. P.; Chwee, T. S.; Fan, W. Y., Highly-phosphorescent tungsten(0) carbonyl pyridyl-imidazole complexes as photosensitisers. *Dalton Trans.* **2017,** *46*, 11008–11012.

(11) Ranieri, A. M.; Burt, L. K.; Stagni, S.; Zacchini, S.; Skelton, B. W.; Ogden, M. I.; Bissember, A. C.; Massi, M. Anionic Cyclometalated Platinum(II) Tetrazolato Complexes as Viable Photoredox Catalysts. *Organometallics* **2019**, *38*, 1108–1117.

(12) Still, W. C.; Kahn, M.; Mitra, A. Rapid chromatographic technique for preparative separations with moderate resolution. *J. Org. Chem*. **1978**, *43*, 2923–2925.

(13) Sheldrick, G. M. *SHELXT* - Integrated space-group and crystal-structure determination. *Acta Cryst.* **2015**, *A71*, 3–8.
(14) Dolomanov, O. V.; Bourhis, L. J.; Gildea, R. J.; Howard, J. A. K.; Puschmann, H. *OLEX2*: a complete structure solution, refinement and analysis program. *J. Appl. Cryst.* **2009**, *42*, 339–341.
(15) Crosby, N.; Demas, J. N. Measurement of photoluminescence quantum yields. *J. Phys. Chem.* **1971**, *75*, 991–1024.
(16) Katsumi, N. Synthesis, Luminescence Quantum Yields, and Lifetimes of Trischelated Ruthenium(II) Mixed-ligand Complexes Including 3,3′-Dimethyl-2,2′-bipyridyl. *Bull. Chem. Soc. Jpn.* **1982**, *55*, 2697–2705.
(17) Frisch, M.; Trucks, G.; Schlegel, H.; Scuseria, G.; Robb, M.; Cheeseman, J.; Scalmani, G.; Barone, V.; Petersson, G.; Nakatsuji, H.; et al. Gaussian 16. Gaussian, Inc. Wallingford, CT: 2016.
(18) Chai, J. D.; Head-Gordon, M. Long-range corrected hybrid density functionals with damped atom–atom dispersion corrections. *Phys. Chem. Chem. Phys.* **2008**, *10*, 6615–6620.
(19) Weigend, F.; Ahlrichs, R. Balanced basis sets of split valence, triple zeta valence and quadruple zeta valence quality for H to Rn: Design and assessment of accuracy. *Phys. Chem. Chem. Phys.* **2005**, *7*, 3297–3305.
(20) Marenich, A. V.; Cramer, C. J.; Truhlar, D. G. Universal solvation model based on solute electron density and on a continuum model of the solvent defined by the bulk dielectric constant and atomic surface tensions. *J. Phys. Chem. B* **2009**, *113*, 6378–6396.
(21) Iron complex **5** is ESR inactive at room temperature in toluene (3115–3658 G, ~9.69 GHz).
(22) (a) Agarwal, J.; Stanton III, C. J.; Shaw T. W.; Vandezande, J. E.; Majetich, G. F.; Bocarsly, A. B.; Schaefer III, H. F. Exploring the effect of axial ligand substitution (X = Br, NCS, CN) on the photodecomposition and electrochemical activity of $[MnX(N–C)(CO)_3]$. *Dalton Trans.* **2015**, *44*, 2122–2131. (b) Sinha, A.; Wahidue Rahaman, S. M.; Sarkar, M.; Saha B.; Daw P.; Bera J. K. Multifaceted Coordination of Naphthyridine–Functionalized N-Heterocyclic Carbene: A Novel "Ir^{III}(C^N)(C^C)" Compound and Its Evaluation as Transfer Hydrogenation Catalyst. *Inorg. Chem.* **2009**, *48*, 11114–11122. (c) Bens, T.; Boden, P.; Martino-Fumo, P. D.; Beerhues, J.; Albold, U.; Sobottka, S.; Neuman, N. I.; Gerhards, M.; Sarkar, B. Chromium(0) and Molybdenum(0) Complexes with a Pyridyl-Mesoionic Carbene Ligand: Structural, (Spectro)electrochemical, Photochemical, and Theoretical Investigations. *Inorg. Chem.* **2020**, *59*, 15504–15513.
(23) Bonnet, L. G.; Douthwaite, R. E.; Kariuki, B. M. Synthesis of New Chiral N-Heterocyclic Carbene-Imine Ligands and Their Application to an Asymmetric Allylic Alkylation Reaction. *Organometallics* **2003**, *22*, 4187–4189.
(24) Welch, C. J.; Brkovic, T.; Schafer, W.; Gong, X. Performance to burn? Re-evaluating the choice of acetonitrile as the platform solvent for analytical HPLC. *Green Chem.* **2009,** *11*, 1232–1238.
(25) Manuta, D. M.; Lees, A. J. Emission and photochemistry of M(CO)4(diimine) (M = chromium, molybdenum, tungsten) complexes in room-temperature solution. *Inorg. Chem*. **1986**, *25*, 1354–1359. (c).
(26) Mukuta, T.; Simpson, P. V.; Vaughan, J. G.; Skelton, B. W.; Stagni, S.; Massi, M.; Koike, K.; Ishitani, O.; Onda, K. Photochemical Processes in a Rhenium(I) Tricarbonyl N-Heterocyclic Carbene Complex Studied by Time-Resolved Measurements. *Inorg. Chem.* **2017**, *56*, 3404–3413.
(27) (a) Lee, J. J.; Yap, C. P.; Chwee, T. S.; Fan, W. Y. Highly-phosphorescent tungsten(0) carbonyl pyridyl-imidazole complexes as photosensitisers. *Dalton Trans*. **2017**, *46*, 11008–11012. (b) D. M.; Lees, A. J. Photophysics of metal carbonyl complexes. Multiple emissions from diimine-tetracarbonyl complexes of Group VIB metals in room-temperature solution *Inorg. Chem*. **1983**, *22*, 572–573.
(28) On the basis of the photophysical data obtained for, the excited state redox potentials of complexes **1**–**4** were not determined; Lakowicz, J. R. Principles of Fluorescence Spectroscopy, Springer, USA, 3rd Ed., 2010.
(29) (a) Bohnenberger, J.; Feuerstein, W.; Himmel, D.; Daub, M.; Breher, F.; Krossing, I. Stable salts of the hexacarbonyl chromium(I) cation and its pentacarbonyl-nitrosyl chromium(I) analogue. *Nat. Commun.* **2019**, *10*, 624. (b) Bohnenberger, J.; Schmitt, M.; Feuerstein, W.; Krummenacher, I.; Butschke, B.; Czajka, J.; Malinowski, P. J.; Breher, F.; Krossing, I. Completing the triad: synthesis and full characterization of homoleptic and heteroleptic carbonyl and nitrosyl complexes of the group VI metals. *Chem. Sci.* **2020**, *11*, 3592–3603.
(30) Rhenium analogue **F** (Figure 1), does not feature reversible redox behavior in comparison (see: ref. 9).
(31) Qin, Q.; Ren, D.; Yu, S. Visible-light-promoted chloramination of olefins with *N*-chlorosulfonamide as both nitrogen and chlorine sources. *Org. Biomol. Chem*. **2015**, *13,* 10295–10298.
(32) Zhang, X.; Zhu, P.; Zhang, R.; Li, X.; Yao, T. Visible-Light-Induced Decarboxylative Cyclization of 2-Alkenylarylisocyanides with α-Oxocarboxylic Acids: Access to 2-Acylindoles. *J. Org. Chem*. **2020**, *85*, 9503–9513.
(33) Liu, Z.; Nan, X.; Lei, T.; Zhou, C.; Wang, Y.; Liu, W.; Chen, B.; Tung, C.; Wu, L. Photo-induced reductive cross-coupling of aldehydes, ketones and imines with electron-deficient arenes to construct aryl substituted alcohols and amines. *Chin*. *J. Catal*. **2018**, *39*, 487–494.
(34) Ju, X.; Li, D.; Li, W.; Yu, W.; Bian, F. The Reaction of Tertiary Anilines with Maleimides under Visible Light Redox Catalysis. *Adv. Synth. Catal*. **2012**, *354*, 3561–3567.
(35) Lin, S.; Ischay, M. A.; Fry, C. G.; Yoon, T. P. Radical Cation Diels–Alder Cycloadditions by Visible Light Photocatalysis. *J. Am. Chem. Soc* **2011**, *133*, 19350−19353.
(36) Strieth-Kalthoff, F.; James, M. J.; Teders, M.; Pitzer, L.; Glorius, D. Energy transfer catalysis mediated by visible light: principles, applications, directions. *Chem. Soc. Rev*. **2018**, *47*, 7190–7202.
(37) Verhoeven, J. W. Glossary of terms used in photochemistry (IUPAC Recommendations 1996). *Pure Appl. Chem*. **1996**, *68*, 2223–2286.
(38) Singh, K.; Staig, S. J.; Weaver, J. D. Facile Synthesis of *Z*-Alkenes via Uphill Catalysis. *J. Am. Chem. Soc*. **2014**, *136*, 5275–5278
(39) See, for example: Nicholls, T. P.; Bissember, A. C. Developments in Visible-Light-Mediated Copper Photocatalysis. *Tetrahedron Lett.* **2019**, *60*, 150883.

Table of Contents Artwork

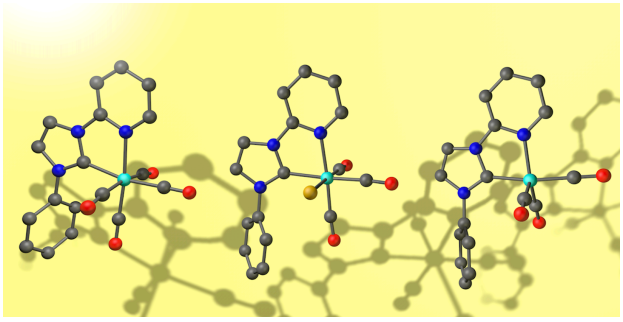

Table of Contents Synopsis

This report details the synthesis and characterization of original, structurally-related chromium, molybdenum, tungsten, manganese, and iron complexes bearing N-heterocyclic carbene and carbonyl ligands. Photophysical studies reveal that decarbonylation occurs in acetonitrile upon exposure to ultraviolet light. To obtain insights into the potential utility, scope, and applications of these complexes in photoredox catalysis, their capacity to facilitate a range of photoinduced reactions was investigated. These chromium, molybdenum, and manganese catalysts efficiently facilitated atom-transfer radical addition processes.